Reduced-Coupling Coestimation of SOC and SOH for Lithium-Ion Batteries Based on Convex Optimization

Dianxun Xiao, *Student Member, IEEE*, Gaoliang Fang, Sheng Liu, Shaoyi Yuan, *Student Member, IEEE*, Ryan Ahmed, *Member, IEEE*, Saeid Habibi, *Member, IEEE*, and Ali Emadi, *Fellow, IEEE*

***Abstract*—Model-based state-of-charge (SOC) and state-of-health (SOH) estimation for lithium-ion batteries has been widely applied in electrified vehicles, while the SOC and SOH estimators are highly coupled and nonlinear in conventional techniques. This leads to a bulky design of observer network and complicates the stability analyses. In this article, a new reduced-decoupling SOC and SOH coestimation algorithm based on convex optimization is proposed. This scheme estimates the battery SOC from the battery model and does not require the classic Coulomb-counting method. Therefore, it can decouple the capacity estimation from the SOC estimator and reduce the strong interaction existing in conventional coestimation methods. Besides, all state variables can be solved together by one estimator, which is straightforward and avoids the complicated observer network. Owing to the decoupling design, the stability of the proposed method becomes more intuitive and can be always guaranteed according to the convexity analysis without using other stabilizing approaches. In consequence, a weak-interaction and robust coestimation algorithm of SOC and SOH can be realized by the proposed technique. The experiments on a 5.4-Ah lithium polymer battery are implemented to validate the feasibility of the algorithm.**

***Index Terms*—Convex optimization, cost function, decoupling, electrified vehicle (EV), lithium-ion battery (LIB), state of charge (SOC), state of health (SOH).**

I. Introduction

LITHIUM-ION batteries (LIBs) attract extensive attention in electrified vehicles (EV) as energy storage components due to their desirable merits such as high power density, high output voltage, and wide operating temperature [1]. A battery pack composes of various LIB cells to generate high power and large capacity; and thus, a battery management system (BMS) is adopted to ensure the battery cells performing in an optimal condition. In the BMS, the prediction of the state-of-charge (SOC) and the diagnostic of the state-of-health (SOH) are the core functions which represent the rest of energy and reflect the battery aging, respectively. As the SOC and SOH are highly coupled in the electrochemical process and hard to be measured, a coestimation technique is required in the BMS.

Currently, existing battery SOC estimation techniques can be categorized into two types [2]: model-free and model-based methods. The Coulomb-counting scheme is the representation of the model-free estimation, which directly derives the SOC by the ampere–hour method. However, its accuracy is significantly degraded by temperature variation, C-rate, initial SOC, and accumulated current sensor errors [3]–[5]. Another direct solution is the open-circuit voltage (OCV) technique which estimates the SOC through the predefined SOC-OCV table [6], while a long rest period is required to stabilize the battery cell. As an alternative, electrochemical impedance spectroscopy (EIS) is measured in impedance spectroscopy methods, and parameters such as ohmic resistance and charge resistance which are parts of SOC function can be analyzed [7]–[9]. Nevertheless, it is sensitive to noises and requires accurate measurement.

Recently, diverse model-free intelligent schemes have been well documented to address the strong nonlinearity and uncertainties of the battery. Fuzzy logic is a typical data-driven scheme to modeling the battery by the nonlinear relationship of input data [10], [11]. For instance, a fuzzy logic system was designed based on the measured EIS data to describe the states-of-battery cells [10]. The authors in [11], employ a fuzzy model to characterize the relationship among the OCV, SOC, and discharge current, and a Kalman filter is further used for state estimation. Besides, strategies involving machine-learning techniques are obtained extensive attention, roughly including support vector machines (SVMs) [12]–[14], and artificial neural networks (ANN) [15]–[17]. In [12], an automated learning tool for SOC prediction was designed based on an SVM for regression, which well estimates the SOC under various operating conditions. In [15], an ANN trained offline by experimental data offers the state-space model for an extended Kalman filter (EKF)-based SOC estimator with high accuracy. Moreover, an enhanced learning-machine technique using recurrent neural network (RNN) with long short-term memory was proposed in [17] to estimate the SOC under different ambient conditions. However, the accuracy of the data-driven schemes relies on the

Manuscript received September 16, 2019; revised December 12, 2019; accepted March 24, 2020. Date of publication April 1, 2020; date of current version July 20, 2020. Recommended for publication by Associate Editor S. Williamson. *(Corresponding author: Gaoliang Fang.)*

Dianxun Xiao, Gaoliang Fang, Sheng Liu, Shaoyi Yuan, and Ali Emadi are with the Department of Electrical and Computer Engineering, McMaster University, Hamilton, ON L8S 4L8, Canada (e-mail: xiaod6@mcmaster.ca; fangg3@mcmaster.ca; liushengneil@gmail.com; yuans20@mcmaster.ca; emadi@mcmaster.ca).

Ryan Ahmed and Saeid Habibi are with the Department of Mechanical Engineering, McMaster University, Hamilton, ON L8S 4L8, Canada (e-mail: mohamerm@mcmaster.ca; habibi@mcmaster.ca).

Color versions of one or more of the figures in this article are available online at http://ieeexplore.ieee.org.

Digital Object Identifier 10.1109/TPEL.2020.2984248

size and quality of training sets, which requires more work on offline data measurement and testing.

Model-based SOC estimation strategies can offer better robustness to uncertainties and noises with less offline tuning effort, which have been emphasized in EV applications. These methods combine the battery model with the Coulomb counting to recalibrate the estimated SOC, thereby reducing the integration errors. This category includes proportional-integral (PI) observer [18], H-infinity filter [19], and Kalman filter [20]–[26], and particle filter [27], [28]. In [18], PI controllers were adopted to converge the voltage prediction error and recalibrate the SOC estimation in the coulomb counting process. The method is concise and robust to initial SOC values, while the model nonlinearity and noises can easily degrade the performance. To enhance the estimation accuracy, various advanced observation techniques are therefore proposed to replace the classic PI controllers. In [19], an H-infinity filter with optimal gains was applied to reduce the adverse impacts of colored noises and increase the SOC estimation accuracy. Furthermore, Kalman filters that are optimum state estimator against white Gaussian noises are emphasized in the battery SOC estimation. Among these, the EKF shows good adaptation and robustness to model nonlinearity and thus was used for SOC estimation based on advanced battery models in [20]–[23]. To improve the robustness to parameter variation and system noises further, adaptive EKFs (AEKF) that adaptively updates the measurement and process noise covariance were implemented in [24]–[26]. Moreover, particle filters can be used to replace the Kalman filter in the applications where non-Gaussian noises are dominant. The successful applications can be found in estimating the SOC and battery parameters [27], as well as the maximum available power state [28]. In summary, most of the model-based techniques adopt a standard *prediction–correction* structure, that is, the Coulomb-counting scheme combined with the battery model predicts the states, and the error-driven observer is employed as a corrector to converge the prediction errors. However, when the battery cell is aged, the capacity and internal resistance would deviate from the nominal values, which lead to large SOC estimation errors. Therefore, it is essential to consider the battery aging, namely, the SOH, when estimating the SOC.

The battery SOH can be expressed by either the internal resistance or the maximum capacity, which can be indirectly estimated. Practically, a doubled internal resistance or a twenty-percent capacity fade represents the fully aging [36]. To estimate the two parameters in real-time applications, model-based SOH estimation schemes together with SOC estimation are widely analyzed in the literature. In [29], Hu, *et al.* proposed a multiscale framework with dual EKFs to estimate the SOC and capacity on two time-scales, where the micro EKF takes charge of SOC estimation in every sampling cycle, and the slowly-varying macro EKF estimates the capacity. Due to the highly coupled capacity and SOC coestimation, the dual EKF should be carefully designed to minimize the mutual influence. Another multi time-scale SOC and SOH coestimation based on nonlinear predictive filters were analyzed in [30], where two coupled nonlinear observers for SOC and capacity estimation are also required. As an alternative, sliding-mode observers (SMO), such as integral-type terminal SMO and dual-SMO in [31] and [32], respectively, represent the coestimation method on the same time scales. All the terminal voltage, OCV, polarization voltage, internal resistance, and capacity are estimated by five highly coupled SMO, and the design for numerous parameters is complicated. In [33], authors proposed a more straightforward solution combining the EKF for SOC estimation and a recursive least square (RLS) algorithm for SOH estimation. Although the coupling issue still exists, the algorithm becomes more compact.

To summarize, the SOC and SOH estimation methods in the literature are highly nonlinear and coupled. Due to the strong dependence of SOC estimation on battery capacity, the insufficient precision of capacity diagnostic may further reduce the SOC estimation accuracy. It significantly increases the difficulty in observer design since several interactive observers/filters should be taken into consideration; but more importantly, much more attention needs to be paid into stability analyses due to the complicated feedback paths. However, local stability and global stability cannot be easily guaranteed simultaneously due to the high complexity of coestimation methods. Therefore, it is necessary to propose a new coestimation solution with weak coupling and robust stability, thereby simplifying the algorithm by fewer observers.

In this article, a new reduced-coupling SOC and SOH coestimation scheme based on convex optimization is proposed. The proposed method abandons the classic prediction–correction structure in conventional methods but estimates the battery SOC/SOH in a new perspective, i.e., numerical optimizer. This approach can solve the optimal solutions of the battery model equations by a numerical searching technique. In detail, a cost function of SOC errors and internal resistance errors is built as a target function. By searching the local minimum of the cost function with a multiple-step Newton's method, the estimation errors can be minimized, and optimal estimates of SOC and internal resistance can be found in each sampling cycle. Afterward, the capacity is estimated separately according to the estimated SOC. Compared to conventional schemes, the proposed approach has several advantages.

1) It essentially decouples the SOC estimation and capacity estimation. The proposed technique directly solves the SOC through the battery model equations, without the usage of the Coulomb-counting method to accumulate the SOC. Therefore, the battery capacity can be decoupled from the SOC estimation as an independent variable, and the strong interaction between the SOC estimation and capacity estimation is eliminated.
2) All the state variables, such as SOC, capacity, and internal resistance, can be estimated by one optimization solver, which avoids the complicated observer network design, e.g., five sliding-mode observers adopted in [31] and [32], and reduces the number of tunable parameters.
3) The global stability of the proposed numerical solver is always guaranteed due to the global minimum in the convexity region. Therefore, no additional stabilized designs (such as widely applied Lyapunov candidate functions) are required, which further simplifies the estimator and benefits the implementation.

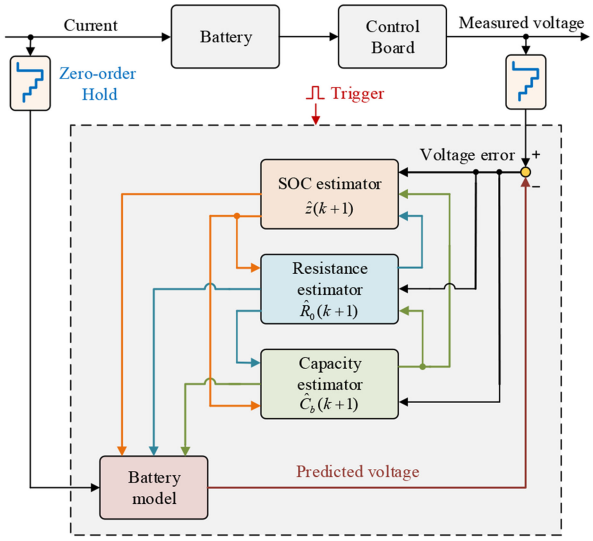

Fig. 1. Block diagram of conventional SOC and SOH coestimation methods.

To validate the feasibility of the proposed SOC and SOH coestimation algorithm, experimental tests based on a 5.4 Ah Lithium polymer battery cell are implemented with real-time drive cycles.

II. Conventional Model-Based SOC/SOH Coestimation Methods

Model-based battery SOC and SOH coestimation techniques offer high estimation accuracy and robust performance, which make them more suitable for EV applications. A general block diagram of the conventional model-based coestimation scheme is shown in Fig. 1. The battery current and terminal voltage are measured by sensors, and zero-order holders denote the digital sampling system in which input signals (current and voltage) are sampled at a fixed frequency.

In conventional coestimation approaches, the Coulomb-counting method is often used to accumulate the battery SOC by ampere–hour integration, which can be expressed in the discrete form at the kth sampling cycle

$$\hat{z}(k+1) = \hat{z}(k) - \frac{i_b(k)\,\Delta T}{\hat{C}_b(k)} + F\left[V_T(k) - \hat{V}_T(k)\right] \quad (1)$$

where the circumflex '^' denotes the estimated variable, z is the SOC, i_b is the input current, C_b is the battery capacity, V_T is the terminal voltage, ΔT is the sampling period, and $F(\cdot)$ represents the observer function. Then, a voltage equation $E(\cdot)$, which is varied according to the battery model, is used to predict the terminal voltage, as follows:

$$\hat{V}_T(k+1) = E\left[\hat{z}(k+1), i_b(k), \hat{R}_0(k+1)\right]. \quad (2)$$

where R_0 is the internal resistance of the battery. The prediction error between the measurement $V_T(k+1)$ and prediction $\hat{V}_T(k+1)$ can be used for the observer $F(\cdot)$ to force the SOC estimate to converge.

As observed in (1) and (2), the SOH represented by the internal resistance and capacity has influence on the SOC estimation; therefore, additional observers are required to estimate the two variables. As a standard approach in the literature, the nonlinear observer with different structures and gains, i.e., $F_1(\cdot)$ and $F_2(\cdot)$, are applied to configure the resistance and capacity estimators, as follows:

$$\hat{R}_0(k+1) = \hat{R}_0(k) + F_1\left[V_T(k) - \hat{V}_T(k), \hat{z}(k), \hat{C}_b(k), \ldots\right] \quad (3)$$

$$\hat{C}_b(k+1) = \hat{C}_b(k) + F_2\left[V_T(k) - \hat{V}_T(k), \hat{z}(k), \hat{R}_0(k), \ldots\right]. \quad (4)$$

The estimated SOH variables are further used in the SOC estimation (1) and (2) to improve the estimation accuracy when the battery cell is aged. As can be seen, the SOC and SOH estimations are highly coupled and affected by each other.

Although various observers and filters in the literature can offer good estimation accuracy, the highly interactive SOC and SOH estimations would complicate the observer design. First, several nonlinear estimators should be separately designed for SOC, internal resistance, and capacity estimations, and each of them would involve different observer structures and gains to ensure local stability. Then, the global stability issue needs to be taken into account due to the coupling and nonlinearity. Moreover, the steady state and dynamic performance of each estimate state is also strongly interactive and requires careful parameter tradeoff design. Accordingly, it is valuable to simplify the estimator design by decoupling the SOC and SOH estimations, especially to separate the capacity estimation that is typically used for battery aging diagnostics.

III. Proposed Convex Optimization Based Reduced-Coupling SOC and SOH Coestimation Scheme

As the SOC and SOH coestimation is a multiobjective and nonlinear estimation problem, it is better to use the online optimization technique to simplify the algorithm. In this article, a new convex optimization-based method is implemented to estimate the battery SOC and SOH with reduced couplings. The convex optimization is capable of handling complicated multiobjective optimization problems with a simple structure, and global stability can be easily guaranteed. By using the convex optimization, the intricate prediction–correction-based observer network shown in Fig. 1 is abandoned; instead, the optimal values of estimates can be searched simultaneously in a convex region by using only one numerical solver.

The overall block diagram of the proposed method is shown in Fig. 2. The SOC and internal resistance estimations are implemented through a convex optimization solver based on the battery model, while the capacity is estimated separately according to the estimated SOC. In detail, the outer loop in Fig. 2 represents the kth sampling cycle where the battery current and terminal voltage are sampled, and the battery capacity is calculated independently based on the estimated SOC.

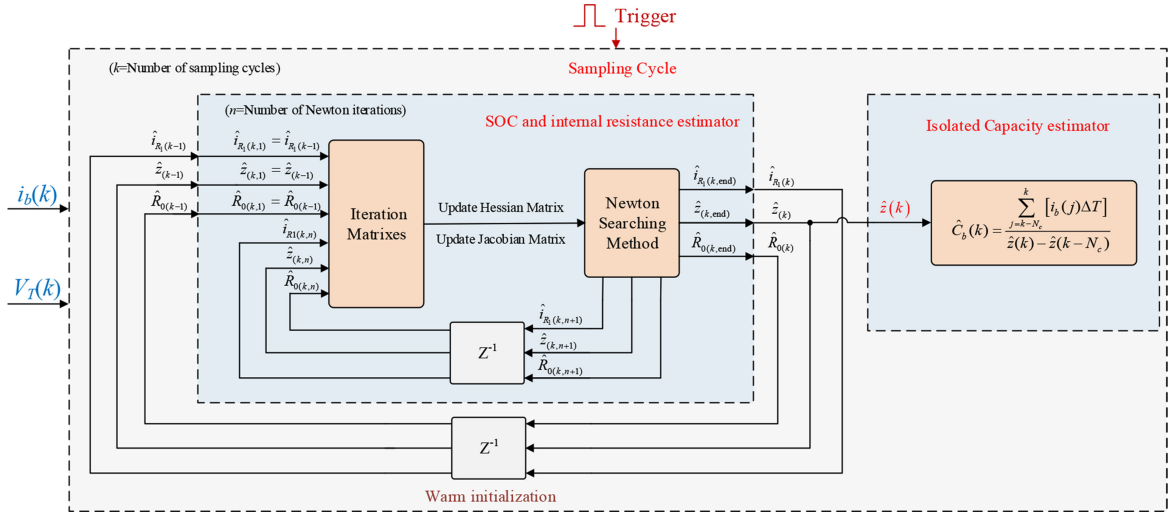

Fig. 2. Overall block diagram of the proposed SOC and SOH coestimation method based on convex optimization.

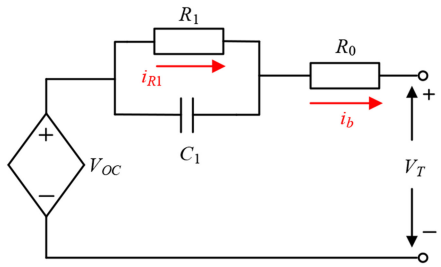

Fig. 3. First-order equivalent circuit battery model.

A Newton searching method is embedded in the sampling cycle to search the local minimum of a cost function (that consists of estimation errors) by n-times iterations. This Newton searching technique helps to directly solve voltage–current differential equations of the battery model and find their optimal numerical solutions, without the usage of ampere-hour integration and additional observers. Thus, the capacity estimator is decoupled from the SOC estimation and the algorithm can be simplified. Moreover, the updated internal resistance can further reduce the adverse impacts of battery aging on the SOC estimate. A robust noise suppression capability is also achieved by the proposed approach, which ensures high estimation accuracy.

A. Cost Function Based on the Battery Model

The article adopts a simple first-order equivalent circuit battery model, as shown in Fig. 3. Battery dynamics are represented by a resistance-capacitor module with an internal resistance in series. According to [38], the model can offer acceptable estimation accuracy, while it has less computational burden. The current and voltage equations of the battery are expressed in discrete form as follows:

$$\begin{cases} V_T(k) = V_{OC}[z(k)] - R_1 i_{R1}(k) - R_0 i_b(k) \\ i_{R1}(k+1) = K_c i_{R1}(k) + (1 - K_c)\, i_b(k) \end{cases} \tag{5}$$

where V_{oc} is the OCV and i_{R1} is the current flowing into the resistor R_1. The K_c is a constant value expressed by $K_c = \exp[-\Delta T/(R_1 C_1)]$. The battery parameters R_0, R_1, and C_1 can be obtained from experimental data using the genetic algorithm (GA). However, the internal resistance has a large variation when the battery cell is aged; and thus, online estimation of the R_0 is required.

The battery SOC and internal resistance can be estimated from the output current and terminal voltage. Conventionally, the SOC estimation is based on the Coulomb-counting method, but in order to decouple the capacity estimation, only the battery model equations, as (5), are used in this article.

In this section, a cost function based SOC and R_0 estimation method is proposed, which can be expressed as

$$G_T(k,n) = G_v^2(k,n) + \lambda_1 G_c^2(k,n) \tag{6}$$

where G_T is the total cost function, G_v is the cost function of the voltage, G_c is the cost function of the polarization-resistor current i_{R1}, and λ_1 is the weighting factor. The (k, n) denotes the cost function in the nth Newton iteration at the kth sampling instant. The G_v and G_c can be derived based on the battery model

$$\begin{cases} G_v(k,n) = V_T(k) - \hat{V}_{OC}[\hat{z}(k,n)] + R_1 \hat{i}_{R_1}(k,n) \\ \qquad\qquad + \hat{R}_0(k,n) i_b(k) \\ G_c(k,n) = \hat{i}_{R_1}(k,n) - K_c \hat{i}_{R_1}(k,n-1) \\ \qquad\qquad - (1 - K_c)\, i_b(k-1). \end{cases} \tag{7}$$

The cost function is aimed to find the optimal solution in each sampling cycle. The battery output current $i_b(k)$ and terminal voltage $V_T(k)$ are first sampled in the kth sampling cycle. The estimated $\hat{i}_{R_1}(k,n)$, $\hat{z}(k,n)$, and $\hat{R}_0(k,n)$ are then updated by n-times Newton searching within the kth sampling interval. If the G_v and G_c can converge to zero, all the estimates will be accurately estimated.

However, in practical applications, measurement noises and fast-varying battery current would degrade the estimation accuracy. To further reduce the noises, the cost function is enhanced

with three state filters, as follows:

$$G_T(k,n) = G_v^2(k,n) + \lambda_1 \left[G_c^2(k,n) + G_{fc}^2(k,n)\right] + \lambda_2 G_{fz}^2(k,n) + \lambda_3 G_{fR}^2(k,n) \tag{8}$$

where G_{fc}, G_{fz}, and G_{fR} are the cost function of the current filter, SOC filter, and internal-resistance filter, respectively.

As the battery voltage, current, resistance, and SOC are on different scales, weight factors should be added to tune the weights of all subcost functions. The $\lambda_{2,3}$ present the weight factors of SOC and resistance estimation filters, respectively. The current filter G_{fc} shares the same weighting factor λ_1 with the G_c as they are on the same scale. A large weight factor of the state filter can offer better noise rejection capability while reducing the response rate. Therefore, the tuning process is a tradeoff but still simple in the proposed method, which will be discussed later.

The subcost functions of filters can reduce the noises in each Newton iteration, as follows:

$$\begin{cases} G_{fc}(k,n) = \hat{i}_{R_1}(k,n) - \hat{i}_{R_1}(k-1) \\ G_{fz}(k,n) = \hat{z}(k,n) - \hat{z}(k-1) \\ G_{fR}(k,n) = \hat{R}_0(k,n) - \hat{R}_0(k-1). \end{cases} \tag{9}$$

Therefore, if the total cost function $G_T(k,n)$ is minimized, all the estimated variables will converge to the actual values.

It is worth noting that if higher order equivalent circuit battery models or other battery models are used, the cost function can be modified accordingly.

B. Newton Searching Technique for the Cost Function

To search the minimum cost function in each sampling cycle, the Newton searching method is adopted. This method can guarantee fast convergence if the convergence trajectory is in a convex region. The searching equations can be expressed as follows:

$$\begin{cases} \delta\hat{\boldsymbol{x}}_{k,n-1} = -\boldsymbol{J}\left(\hat{\boldsymbol{x}}_{k,n-1}\right)/\boldsymbol{H}\left(\hat{\boldsymbol{x}}_{k,n-1}\right) \\ \hat{\boldsymbol{x}}_{k,n} = \hat{\boldsymbol{x}}_{k,n-1} + \delta\hat{\boldsymbol{x}}_{k,n-1} \\ \text{minimize } G_T\left(\hat{\boldsymbol{x}}_{k,n}\right) \end{cases} \tag{10}$$

where $\hat{\boldsymbol{x}}_{k,n} = [\,\hat{i}_{R_1}(k,n)\ \hat{z}(k,n)\ \hat{R}_0(k,n)\,]'$ denotes the estimated state variables in the kth sampling cycle and the nth Newton iteration. $\boldsymbol{H}$ is the Hessian matrix (3×3 matrix), and $\boldsymbol{J}$ is the Jacobian matrix (3×1 matrix), which are the second-order and first-order partial derivatives to the state variables $\hat{\boldsymbol{x}}_{k,n}$ of the cost function, respectively. The matrixes $\boldsymbol{H}$ and $\boldsymbol{J}$ are given by

$$\boldsymbol{H}\left(\hat{\boldsymbol{x}}_{k,n}\right) = \left[\begin{array}{ccc} \frac{\partial^2 G_T}{\partial \hat{i}_{R_1}^2} & \frac{\partial^2 G_T}{\partial \hat{i}_{R_1}\partial \hat{z}} & \frac{\partial^2 G_T}{\partial \hat{i}_{R_1}\partial \hat{R}_0} \\ \frac{\partial^2 G_T}{\partial \hat{z}\partial \hat{i}_{R_1}} & \frac{\partial^2 G_T}{\partial \hat{z}^2} & \frac{\partial^2 G_T}{\partial \hat{z}\partial \hat{R}_0} \\ \frac{\partial^2 G_T}{\partial \hat{R}_0\partial \hat{i}_{R_1}} & \frac{\partial^2 G_T}{\partial \hat{R}_0\partial \hat{z}} & \frac{\partial^2 G_T}{\partial \hat{R}_0^2} \end{array}\right]\Bigg|_{(k,n)} \tag{11}$$

$$\boldsymbol{J}\left(\hat{\boldsymbol{x}}_{k,n}\right) = \left[\begin{array}{ccc} \frac{\partial G_T}{\partial \hat{i}_{R_1}} & \frac{\partial G_T}{\partial \hat{z}} & \frac{\partial G_T}{\partial \hat{R}_0} \end{array}\right]'\Bigg|_{(k,n)} \tag{12}$$

where

$$\begin{cases} H_{11} = 2R_1^2 + 2\lambda_1 + 2\lambda_2, \\ H_{12} = -2R_1\frac{dV_{oc}}{d\hat{z}}, H_{13} = 2R_1 i_b \\ H_{21} = H_{12},\ H_{22} = 2\left(\frac{dV_{oc}}{d\hat{z}}\right)^2 - 2G_v\frac{d^2V_{oc}}{d\hat{z}^2} + 2\lambda_3, \\ H_{23} = -2i_b\frac{dV_{oc}}{d\hat{z}}, H_{31} = H_{13},\ H_{32} = H_{23}, \\ H_{33} = 2i_b^2 + 2\lambda_4 \end{cases}$$

$$\begin{cases} J_1 = 2R_1G_v + 2\lambda_1 G_c + 2\lambda_2 G_{fc}, \\ J_2 = -2G_v\frac{dV_{oc}}{d\hat{z}} + 2\lambda_3 G_{fz} \\ J_3 = 2G_v i_b + 2\lambda_4 G_{fR}. \end{cases}$$

H_{xy} and J_x, (x and $y = 1,2,3$) are the elements of the matrixes. The derivative of the OCV over the estimated SOC can be calculated by polynomials or stored by lookup tables.

By (10), a descending direction can be defined to search the local minimum of the cost function by n-times Newton iterations. Due to the Newton minimization being embedded in the kth sampling cycle, the battery output current $i_b(k)$ and terminal voltage $V_T(k)$ keep constant when the Newton iteration is implementing. Only the state variables $\hat{\boldsymbol{x}}_{k,n}$ are updated n times until reaching the maximum number of iterations or satisfying an acceptable tolerance η_x. This ending condition of the Newton searching in the kth sampling cycle can be expressed as

$$\boldsymbol{if}\ \ (n = \text{max No. of iterations}) \cup \left(G_T(\hat{\boldsymbol{x}}_{k,n}) < \eta_x\right). \tag{13}$$

The proposed Newton searching method is depicted in detail in Fig. 2. At the end of the Newton iteration, the newest updated variables $\hat{\boldsymbol{x}}_{k,\text{end}}$ are set as the optimal estimation outputs, i.e., $\hat{\boldsymbol{x}}_k = \hat{\boldsymbol{x}}_{k,\text{end}}$. In the next sampling period, the Newton searching is reapplied and iterated again from $n = 1$ to its ending condition (13) based on the $(k+1)$th sampled current and terminal voltage. Furthermore, to achieve the warm initialization that can accelerate the iteration, the estimated values in the previous sampling cycle are set as the initial values of the Newton searching in the next sampling cycle.

By the proposed Newton searching approach, the local minimum of the cost function can be found in each sampling period. The estimated variables, including SOC and internal resistance that minimize the cost function, can be regarded as the optimal results. Moreover, the capacity value is not used in the proposed optimization process, and thus the strong coupling between the SOC and capacity estimation is eliminated. Although the internal resistance R_0 still has some couplings with the SOC estimation, it can be estimated together with the SOC by simply adding a subcost function $\lambda_3 G_{fR}^2(k,n)$ in (8). Therefore, the proposed technique does not require a separated design of the resistance estimator, thereby avoiding the sophisticated observer network and simplifying the algorithm and its implementation.

C. Capacity Estimation

The battery capacity can be estimated separately and then used for aging diagnostic. A simple way analyzed in [33] is adopted

in this article, as

$$\hat{C}_b(k) = \frac{\sum_{j=k-N_c}^{k} [i_b(j)\Delta T]}{\hat{z}(k) - \hat{z}(k-N_c)} \tag{14}$$

where the accumulated current over the SOC difference in N_c sampling cycles is used for capacity estimation. Considering the battery aging is a slowly time-varying state, N_c can be chosen as large as possible or employing a low-pass filter to obtain a stable and ripple-free estimated capacity.

IV. Convexity and Stability Analysis

Generally, the cost function can be minimized to zero if all convergence trajectories are in a convex region. Therefore, in order to prove the stability and convergence of the proposed optimization method, the convexity of the cost function should be analyzed.

A. Cost Function With Only Current Filter

The unique local minimum of the cost function is necessary to avoid the ambiguous convergence. The ideal local minimum points should be around the zero-estimation-error point that indicates the estimation is accurate. To analyze the distribution of the cost function, the estimated values at the $(k-1)$th sampling instant are regarded as the actual values, and the estimation errors are considered at the kth instant [34]

$$\begin{cases} \hat{\boldsymbol{x}}_{k-1} = \boldsymbol{x}_{\text{act}} \\ \hat{\boldsymbol{x}}_{k,n} = \boldsymbol{x}_{\text{act}} + \Delta \boldsymbol{x}_{k,n} \end{cases} \tag{15}$$

where $\boldsymbol{x}$ is the state variables the same as (10), and $\Delta\boldsymbol{x}$ denotes the estimation error. It can establish a relationship between the cost function and estimation errors at each sampling cycle. The SOC-OCV curve of the experimental battery cell and weight factors are given in Section V.

For the sake of simplicity, the cost function in (8) without the SOC and resistance filters is first analyzed. According to (15), the cost function in (8) can be rewritten by removing the last two terms and considering the estimation errors, as follows:

$$G_T(\Delta) = G_v^2(\Delta) + \lambda_1 \left[G_c^2(\Delta) + G_{fc}^2(\Delta)\right] \tag{16}$$

where $\Delta = [\Delta i_{R_1}, \Delta z, \Delta R_0]$. The $G_v(\boldsymbol{\Delta})$, $G_c(\boldsymbol{\Delta})$, and $G_{fc}(\boldsymbol{\Delta})$ can be expressed by

$$\begin{cases} G_v(\Delta) = \hat{V}_{OC}[z_{\text{act}}(k)] - \hat{V}_{OC}[z_{\text{act}}(k) + \Delta z(k,n)] \\ \qquad\qquad - R_1 \Delta i_{R_1}(k,n) - \Delta R_0(k,n) i_b(k) \\ G_c(\Delta) = -\Delta i_{R_1}(k,n) + k_c \Delta i_{R_1}(k,n-1) \\ G_{fc}(\Delta) = \Delta i_{R_1}(k,n). \end{cases} \tag{17}$$

Due to the cost function $G_T(\boldsymbol{\Delta})$ always being nonnegative, it can be easily found that when $G_v^2(\Delta)$, $\lambda_1 G_c^2(\Delta)$, and $\lambda_1 G_{fc}^2(\Delta)$ are all zero, the local minimum values of $G_T(\boldsymbol{\Delta})$ will be zero as well. Therefore, the local minimum coordinates satisfy the following expressions

$$\begin{cases} \hat{V}_{OC}[z_{\text{act}}] - \hat{V}_{OC}[z_{\text{act}} + \Delta z] + \Delta R_0 i_b = 0 \\ \Delta i_{R_1} = 0 \end{cases} \tag{18}$$

where the marks of instants, such as (k) and (k,n), are removed for convenience. It is intuitive that there would be multiple local minimums $\Delta_i = [0, \Delta z_i, \Delta R_{0,i}]$ in (18), which may lead to incorrect convergence.

To analyze the convergence of the optimization, the convexity should be investigated. If the cost function is locally convex, the initial states that locate in the convex region can converge to the local minimums. Also, if the global convexity of the cost function can be guaranteed, the local minimum will be the global minimum that can be reached within finite iterations [35]. The cost function $G_T(\boldsymbol{\Delta})$ is said to be convex when its Hessian matrix $\boldsymbol{H}$ given in (11) is positive semidefinite. This positive semidefinite of $\boldsymbol{H}$ can be defined when all the leading principal minors of $\boldsymbol{H}$ are positive, which yields

$$\begin{cases} m_1 = H_{11} > 0,\ m_2 = \begin{vmatrix} H_{11} & H_{12} \\ H_{21} & H_{22} \end{vmatrix} > 0 \\ m_3 = |\boldsymbol{H}| > 0 \end{cases} \tag{19}$$

where $|\bullet|$ denotes the determinant of a matrix. For the cost function (16), the λ_2 and λ_3 are zero when calculating $\boldsymbol{H}$ in (19).

However, due to the high complexity of the Hessian matrix, it is challenging to solve (19) analytically. In the proposed method, the convex region of the cost function, as well as the solutions of (18), are illustrated by plotting. An arbitrary operating condition of the battery cell is chosen as an example, where the actual values of the states are $z_{\text{act}} = 50\%$, $R_{0\text{act}} = 0.01\ \Omega$, and $i_{R1\text{act}} = 2$ A, as well as the battery current being $I_{\text{bact}} = 10$ A. The SOC error Δz ranges from -50% to 50%, the resistance error ΔR_0 is considered from -10 to 10 mΩ, and the current error Δi_{R_1} is zero because of (18). The numerical results by solving (18) and (19) are shown in Fig. 4(a). In the case where no SOC and resistance filters are considered, the solutions of (18) are not unique and distribute in various SOC errors and resistance errors. These solutions are all the local minimums of the cost function as they are confined with the convex region depicted by the gray area. The convergence to the local minimums can be guaranteed if the estimation errors are within the convex region. However, the infinite local minimums lead to incorrect convergent results that are not around the original. Outside the convex region, no convergence guarantees can be issued [34].

Therefore, the convex optimization cannot be ensured if the cost function without the SOC and resistance filters is adopted.

B. Cost Function With Both Current and SOC Filters

As aforementioned in (18), the cost function without the SOC and resistance filters can only ensure the current estimation error being zero. The infinite local minimums of the SOC and resistance estimates can be eliminated by adding a SOC estimation filter to the previous cost function (16), which gives

$$G_T(\Delta) = G_v^2(\Delta) + \lambda_1 \left[G_c^2(\Delta) + G_{fc}^2(\Delta)\right] + \lambda_2 G_{fz}^2(\Delta) \tag{20}$$

where the SOC filter considering estimation errors is expressed by

$$G_{fz}(\Delta) = \Delta z. \tag{21}$$

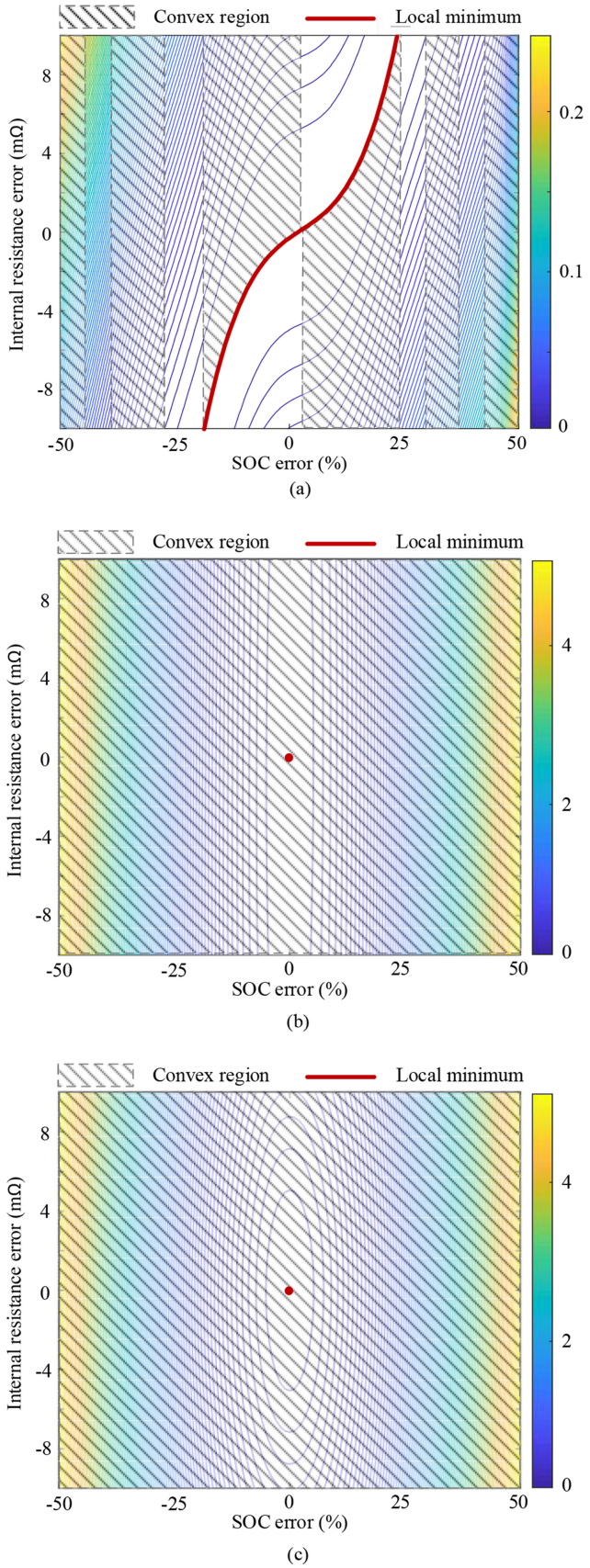

Fig. 4. Contour plots of the three cost functions and the convex region. (a) With only the current filter. (b) With both the current and SOC filters. (c) With all filters.

The SOC filter offers a certain local minimum value for SOC estimation, that is $\Delta z = 0$ when $\lambda_2 G_{fz}^2(\Delta) = 0$. Therefore, the issue of the infinite local minimums is solved, and the unique convergence result can be ensured. To verify it and analyze the convex region, the numerical analysis by plotting is also conducted, as shown in Fig. 4(b). It is evident that the cost function reduces along with the decrease of the estimation errors, and there is only one optimal solution where the estimation errors are both zero. As the convexity is guaranteed in the whole region, the local minimum becomes the global minimum, and all the initial states can finally converge to the global minimum within finite iterations. Therefore, the estimation is an online nonlinear optimization issue which can be solved by lessening the proposed cost function.

However, the gradient, along with the R_0 error-axis, is quite small, which means a minor disturbance on the estimated internal resistance would lead to a long convergence time or even infinite the convergence process. Thus, the estimator is not active if using this cost function.

C. Cost Function With All Current, SOC and Resistance Filters

As an improvement, the internal-resistance filter is also considered in this article, which is the final design that has been mentioned in (8). The finalized cost function is recalled here with the consideration of estimation errors, as follows:

$$G_T(\Delta) = G_v^2(\Delta) + \lambda_1 \left[G_c^2(\Delta) + G_{fc}^2(\Delta)\right] + \lambda_2 G_{fz}^2(\Delta) + \lambda_3 G_{fR}^2(\Delta). \quad (22)$$

This filter $\lambda_3 G_{fR}^2(k,n)$ has no effect on the local minimum as it also gives the $\Delta R_0 = 0$, but it can improve the robustness to the noises and improve the resistance estimation accuracy. Fig. 4(c) shows the contour plots and the convex region of the cost function (22). Compared to Fig. 4(b) where no internal-resistance filter is used, the gradient along the resistance error increases a lot, and there is no effect for the SOC estimation. The proposed method can thereby quickly converge the resistance errors with strong robustness to the external disturbance.

V. Experimental Results

A. Experimental Setup and Testing Conditions

To validate the feasibility of the proposed SOC and SOH coestimation technique, experiments are performed based on a 5.4-Ah Lithium polymer battery cell. The detailed nominal specifications and the weight factors of the cost function are listed in Table I. The experimental setups are as shown in Fig. 5, including three-channel Arbin BT2000 tester and two environmental chambers. All data were measured by an Arbin cycler at a sampling frequency of 10 Hz.

The measured SOC-OCV relationship is depicted in Fig. 6. This feature is captured by a constant–current-constant–voltage (CCCV) test, where a small C-rate (C/15) is used to charge and discharge the battery cell to minimize battery dynamics and ohmic losses, and then the average of the discharging and

TABLE I
PARAMETERS OF THE TESTED BATTERY AND THE COST FUNCTION

Parameter	Value
Type	Lithium polymer cell
Nominal voltage	3.7 V
Nominal capacity	5.4 Ah
Nominal current	2.7 A
λ_1	50
λ_2	20
λ_3	2000

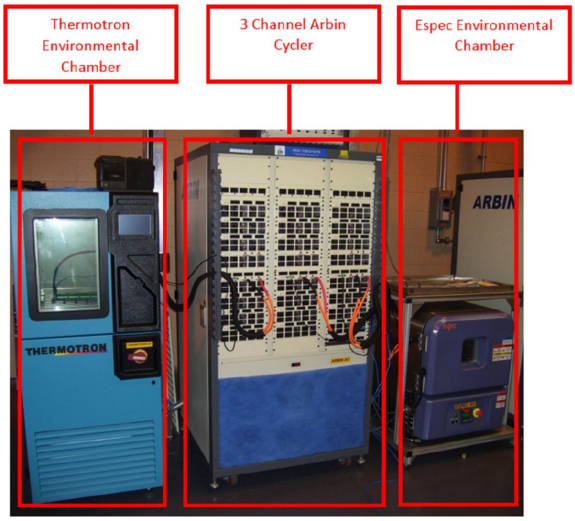

Fig. 5. Experimental setups.

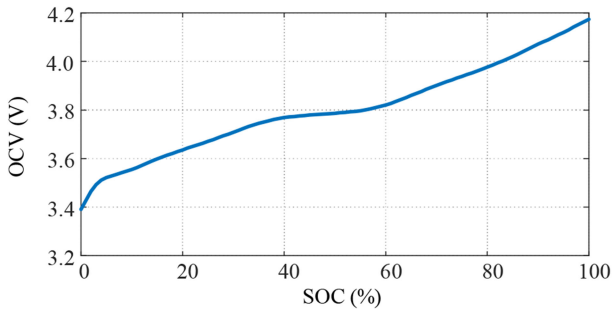

Fig. 6. SOC-OCV relationship for the tested battery.

charging curves are used as the final SOC-OCV characteristic. It is worth noting that the SOC-OCV curve exhibits a flat change in the region between 35% and 52% SOC. This characteristic is more sensitive to measurement noises and increases the challenge to estimate battery SOC in the overall operating range.

In the article, three drive cycles are used for experimental validation. All the reference current waveform is generated from an electric vehicle model under a series of UDDS, US06, and HWFET drive cycles. The drive cycle-A that consists of the battery current ranging from −2 C-rate to 2 C-rate is shown in Fig. 7, where the terminal voltage, battery current, and actual SOC are given. The ambient temperature of the drive cycle-A is 35 °C. This drive cycle is used for initial validation of the proposed coestimation scheme. Other two drive cycles with larger C-rate and different ambient temperatures will be introduced later.

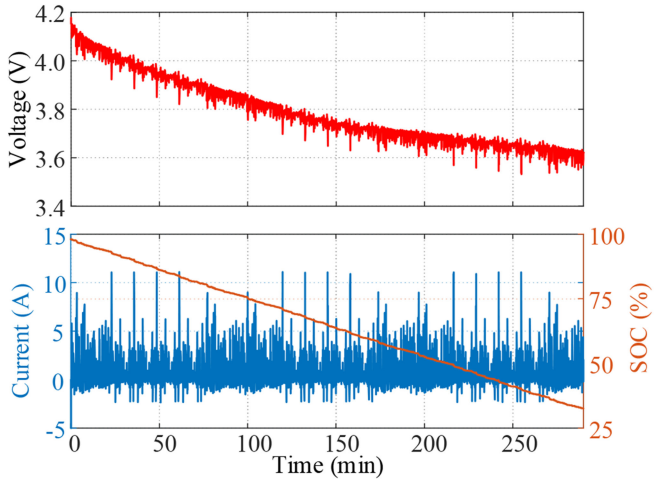

Fig. 7. Drive cycle-A: 2 C-rate @ 35 °C.

B. Verification of the Cost Functions

The experimental results using drive cycle-A is shown in Fig. 8, which verify the proposed cost function design and convexity analyzed in Section IV. The initial SOC is set at 50%, and several cost functions are compared by experiments. In Fig. 8(a), the proposed cost function with all state filters in (22) is first adopted, while the cost function with only the current filter in (16) is applied at 145 min for comparison purpose. As can be seen, the proposed cost function containing all state filters has a convergent SOC estimation result, but the estimation becomes unstable after removing the SOC and resistance filters due to the infinite and uncertain local minimums, as shown in Fig. 4(a). Then, the cost function with the current and SOC filters in (20) is verified and enabled at 145 min in Fig. 8(b). Although the issue of multiple local minimums is solved according to Fig. 4(b), the gradient along the R_0-axis, which is close to zero, leads to a long convergence process, and the estimated SOC is even unchanged after 145 min.

Accordingly, all the state filters are required to guarantee the global minimum and convexity, and the overall estimated SOC with the proposed cost function is shown in Fig. 8(c). The absolute SOC error is shown in the figure, and the root-mean-square error (RMSE) is 1.467% that can be calculated by

$$\mathrm{RMSE} = \sqrt{\frac{\sum_{i=1}^{N} \left(\hat{z}_i - z_{\mathrm{act},i}\right)^2}{N}}. \tag{23}$$

Meanwhile, the proposed method can converge the SOC estimate from the initial 50% SOC error to zero in a relatively short time of 12 s.

In addition, the SOH estimation represented by the internal resistance and capacity is shown in Fig. 8(d). From the results, the estimated internal resistance can match the offline identification value, that is 11.5 mΩ by the GA. The battery capacity can be calculated separately in (14) by the accumulated current over the difference of the estimated SOC between two time points, where N_c is set as 87 000 that denotes 8700 s (sampling period equal to 0.1 s) in this article. It is worth noting that the selection of N_c has no effect on the optimization algorithm due to the

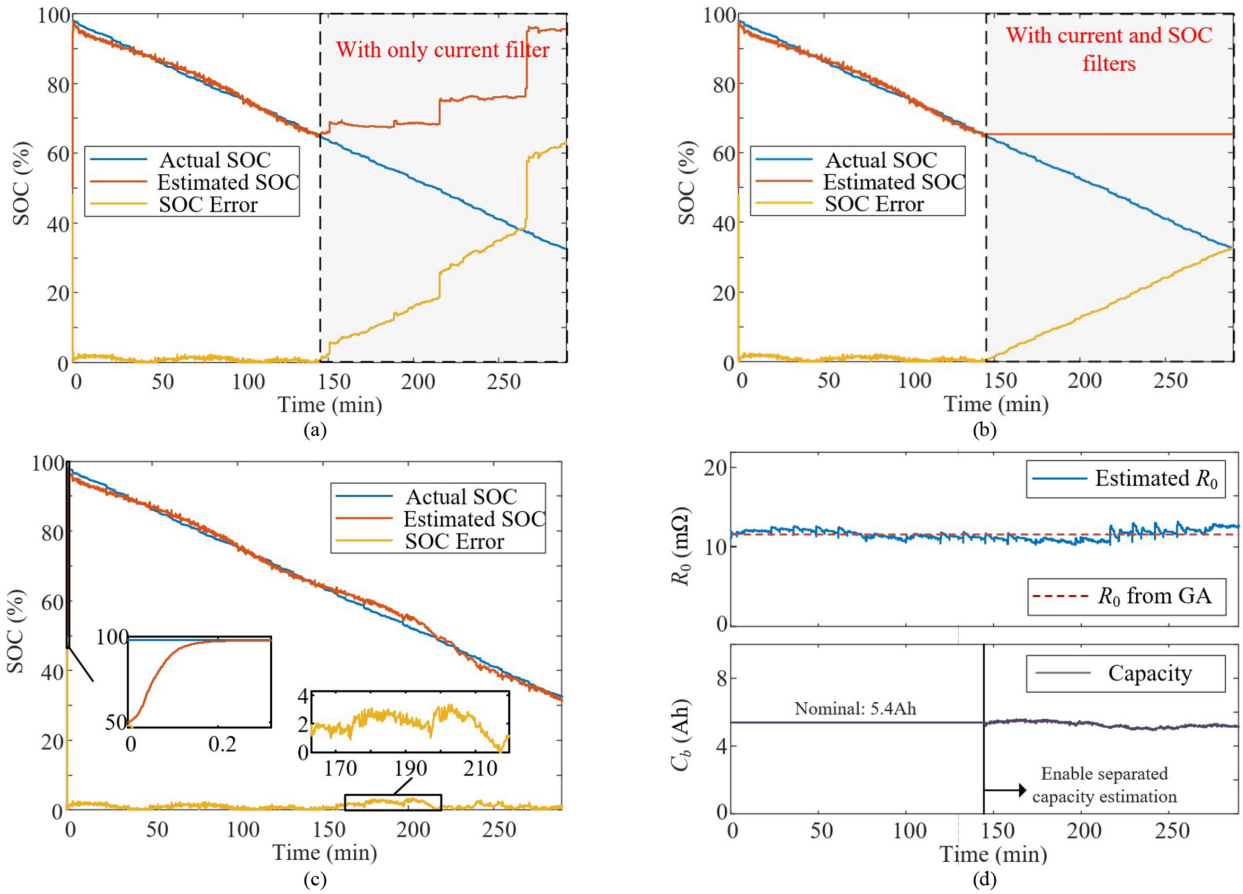

Fig. 8. SOC and SOH coestimation results with different cost functions (drive cycle-A: 2 C-rate @ 35 °C). (a) Cost function (16) with only current filter. (b) Cost function (20) with current and SOC filters. (c) Cost function (22) with all state filters. (d) SOH estimation.

isolated capacity estimation. Before 145 min, the capacity is assumed as its nominal value, and then the capacity estimation is enabled to update the battery aging. It is worth noting that the proposed capacity estimation result has some ripples since less than one drive cycle is used for aging estimation. In actual applications, a higher and ripple-free capacity estimation accuracy can be obtained by increasing the calculation interval N_c or adding a low-pass filter with very low cutoff frequency, as the battery aging is much slow. Therefore, the capacity estimation can be done over several charging/discharging cycles, thereby enhancing the accuracy.

For the proposed method, three weight factors $\lambda_{1,2,3}$ in the total cost function expressed by (8) determine the estimation performance. The tuning process of the parameters is a tradeoff but still simple. First, the weight factor λ_3 for the internal-resistance filter affects the noise suppression of the internal resistance estimation and can be easily assigned. Since the battery aging and temperature variation are slow, the internal resistance R_0 is a slowly time-varying value. A relatively large value of λ_3 can be select to filter out ripples in the internal-resistance estimate $\hat{R}_0$, and thus improving the SOH estimation accuracy. Therefore, the tuning of λ_3 is simple and does not require much effort. Once the λ_3 is assigned, the tuning of other weight factors $\lambda_{1,2}$ is a tradeoff between steady-state and transient estimation accuracy. As the polarization (i.e., the parallel resistor-capacitor element in the battery model) determines the transient modeling accuracy, the large weight factor λ_1 for the polarization-resistor current $\hat{i}_{R_1}$ can enhance the convergence rate, but it would reduce the relative weight of the SOC estimation filter and hence cause the SOC estimation to be more sensitive to noises. Similarly, an excessively large weight factor λ_2 of the SOC estimation filter would suppress the transient performance. Accordingly, if the measurement contains large noises, smaller λ_1 and larger λ_2 are expected to filter the noises in estimates, and vice versa. In the test, the weight factors are set as 50, 20, and 2000, respectively.

To summarize, only two parameters in the cost function need to be tuned according to the specific applications, and other SOH-dependent parameters can be simply configured due to their slow-varying variation and the decoupling achieved by the proposed optimization technique.

C. Selection of the Number of Iterations

As the SOC-OCV relationship is nonlinear, the proposed cost function is not quadratic and thus the algorithm cannot converge within one iteration in every sampling cycle [37]. However, thanks to the convexity proved in Section IV, the proposed optimization-based coestiamtion method can converge in a limited number of iterations. In this section, the selection of the maximum iteration number is analyzed by using

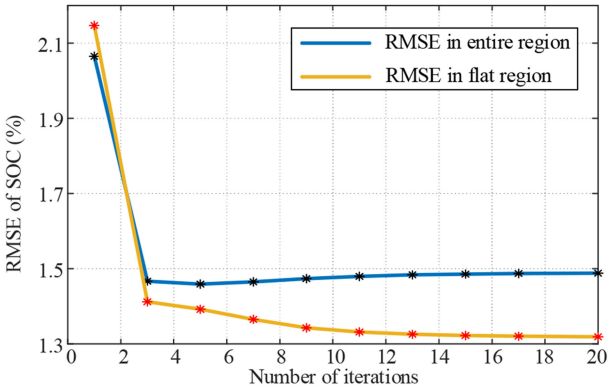

Fig. 9. RMSE of SOC estimation with different numbers of iterations.

experimental data. Fig. 9 compares the RMSE of SOC estimation with different numbers of iterations. When the number of iterations is only one, a larger SOC estimation error can be found in the both the entire and flat regions, which indicates the optimization process can not be completed in one iteration. After selecting the number of iterations to three, the estimated SOC can track the actual value with a smaller RMSE. However, there will be not much improvement on estimation accuracy when further increasing the iteration times. Therefore, three iterations are enough to complete the proposed coestimation algorithm. A larger number of iterations can be selected to further improve the estimation accuracy, especially in the flat region, while the article choses the number of iterations as three, which can offer acceptable accuracy and have less computational burden.

D. Performance Comparison With Other Methods

To show the superiority of the proposed strategy compared to other model-based methods, the estimation results of the existing SOC estimation strategies and coestimation schemes are used for the comparison. The initial SOC values of all schemes are set as 50%. The drive cycle-A is used for the comparative analysis.

Fig. 10 shows the comparative results with PI- [18] and EKF-based [20] SOC estimations, where Fig. 10(a) and (b) are the results for a fresh battery cell, and Fig. 10(c) and (d) depict the estimation by considering battery aging with doubled internal resistance and 20% capacity fade. The parameters are tuned to ensure the same convergence time for all techniques, i.e., 0.2 min (12 s), which means the same dynamic performance; and the SOC estimation errors are used for a fair comparison. In Fig. 10(a), the absolute errors of SOC estimation in both the PI-based and proposed methods are similar in most cases, while the maximum absolute errors (MAE) of the PI-based observer in the flat SOC-OCV region (35%–52%) increases to MAE = 6.831%, and the proposed strategy only has the MAE = 3.367%. This flat feature leads to higher noise sensitivity, and hence it can be used to compare the estimation performance. For the EKF-based scheme, as shown in Fig. 10(b), it has a lower error than the PI-based method, which is MAE = 4.829% in the flat region, but it is still larger than that of the proposed strategy. Furthermore, the SOC estimation errors become worst for the conventional SOC estimation techniques with the mismatched internal resistance and capacity values due to battery aging, as shown in Fig. 10(c) and (d). The battery SOH has a significant influence on the PI- and EKF-based estimators, and large estimation errors appear in all operating range. On the contrary, the proposed convex optimization-based coestimation can online update the SOH, and is thereby capable of tracking the battery aging and maintaining high estimation accuracy. For intuitive comparison, the RMSE and maximum errors for all methods are listed in Table II.

In addition, the proposed coestimation method is compared to other coestimation techniques. In Fig. 11(a), a recent work combining EKF and RLS for SOC and SOH coestimation [33] is used when battery aging happens. The parameter tuning is the same as the single EKF, and the convergence time is also 12 s. Compared to the result of the single EKF in Fig. 10(d), the EKF-RLS-based coestimation can update the battery aging and has higher accuracy than the EKF without tracking the SOH. The proposed method, however, still shows better SOC estimation accuracy in the flat region (RMSE = 1.412%) than the EKF-RLS scheme (RMSE = 2.680%). Another widely concerned coestimation technique, the dual SMO (DSMO) in [32], is used for the comparative experiment considering fully aging, as shown in Fig. 11(b). To reduce the scattering issue in the DSMO, the convergence time cannot be shorter as 12 s, and thereby the parameter tuning of the DSMO is based on the same SOC error after convergence for a fair comparison. As can be observed, although the DSMO can estimate the SOC well by considering the battery aging, the convergence process of the DSMO coestimation method is much longer, which is around 12.5 min. Accordingly, the RMSE over the entire region is 3.610% for the DSMO, which is more significant than 1.459% of the proposed method.

E. Estimation Results With Other Drive Cycles and Ambient Temperatures

The performance of the proposed scheme is further validated with high C-rate drive cycles and under different ambient temperatures. Compared to the previous drive cycle-A (2 C-rate @ 35 °C), the drive cycle-B (10.2 C-rate @ 25 °C) and drive cycle-C (12.5 C-rate @ 25 °C) are used and shown in Figs. 12 and 13, respectively.

Fig. 14 shows the comparative estimation results by using drive cycle-B, of which C-rate = 10.2 C and temperature = 25 °C. All tunable parameters of the proposed method, EKF-RLS, and DSMO are the same as the ones used in the drive cycle-A. The RMSE in the entire drive cycle and the MAE after convergence are summarized in Table III. Since the drive cycle-B does not cover the flat SOC region (35%-52%), the results in the flat region are not listed. As can be seen, the convergence time of the EKF-RLS method and the proposed scheme are still 12 s, due to the unchanged control parameters. The RMSEs of the proposed and EKF-RLS are similar, which are 1.502% and 1.653%, respectively. However, the proposed method has smaller estimation ripples, and the MAE after convergence is 3.214% which is nearly half of the error in the EKF-RLS method (7.056%). Besides, the comparison with the DSMO is also shown.

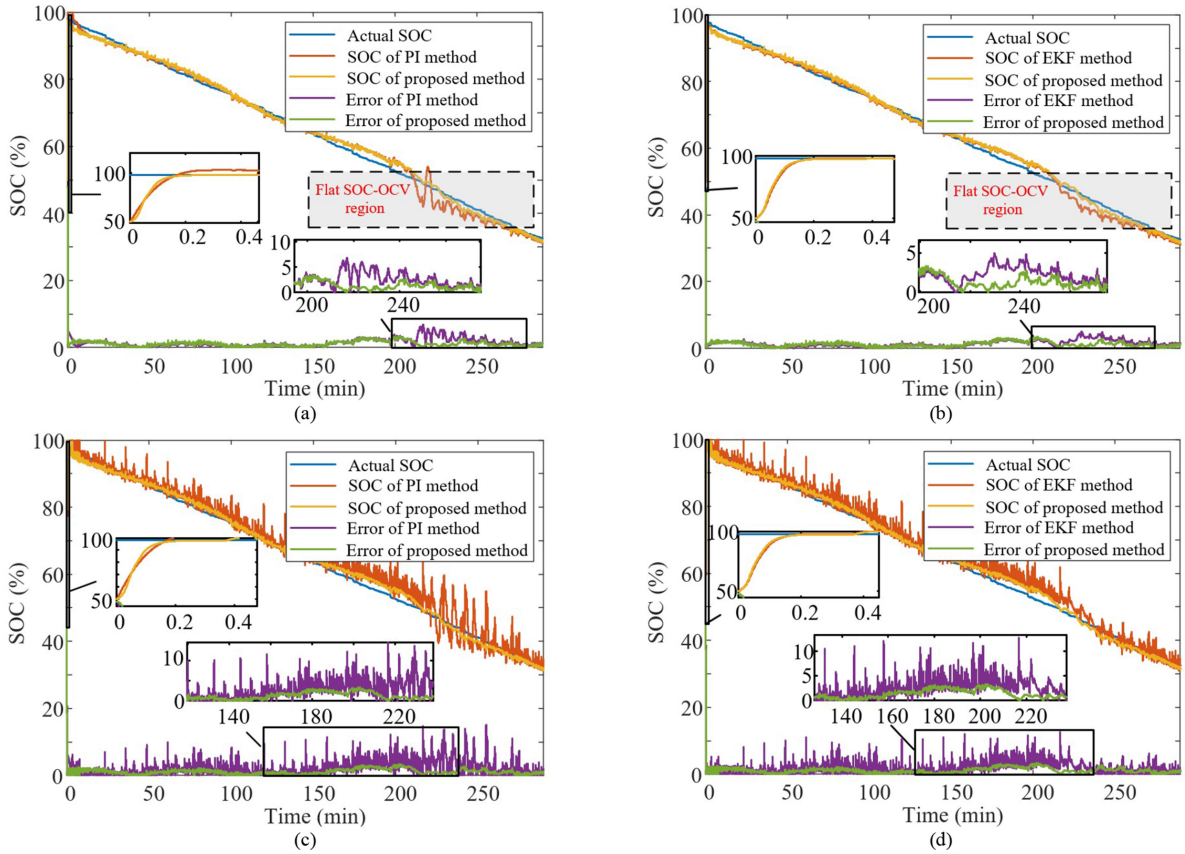

Fig. 10. Comparation between conventional SOC-estimation methods and the proposed method (drive cycle-A: 2 C-rate @ 35 °C). (a) PI-based method on fresh cell. (b) EKF-based method on fresh cell. (c) PI-based method considering battery aging. (d) EKF-based method considering battery aging.

TABLE II
RMSE AND MAE OF SOC ESTIMATION AMONG DIFFERENT TECHNIQUES IN ENTIRE RANGE AND FLAT REGION (DRIVE CYCLE-A: 2 C-RATE @ 35 °C)

Techniques	Convergence Time	Fresh (%)			Aging (%)		
		RMSE (entire)	RMSE (flat)	MAE (flat)	RMSE (entire)	RMSE (flat)	MAE (flat)
PI [18]	12 sec	1.988	3.026	6.831	3.219	4.704	15.14
EKF [20]	12 sec	1.740	2.423	4.829	2.470	2.730	12.72
EKF-RLS [33]	12 sec	1.770	2.563	5.313	1.826	2.680	5.928
Dual SMO [32]	12.5 min	3.702	1.529	4.193	3.610	1.570	4.683
Proposed	12 sec	1.467	1.412	3.367	1.459	1.412	3.367

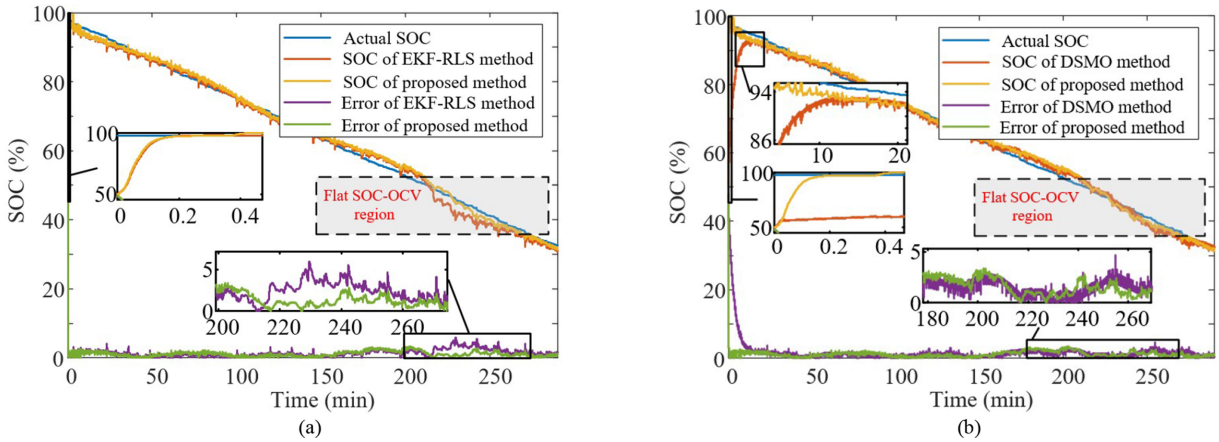

Fig. 11. Comparative experiments with conventional coestimation techniques considering battery aging (drive cycle-A: 2 C-rate @ 35 °C). (a) EKF-RLS. (b) Dual SMO.

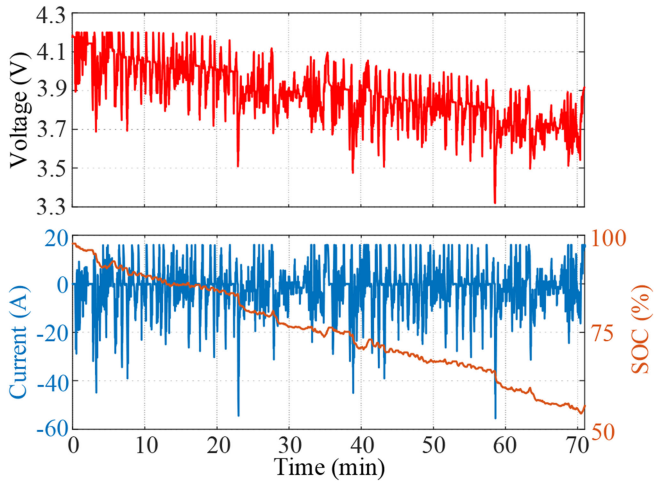

Fig. 12. Drive cycle-B: 10.2 C-rate @ 25 °C.

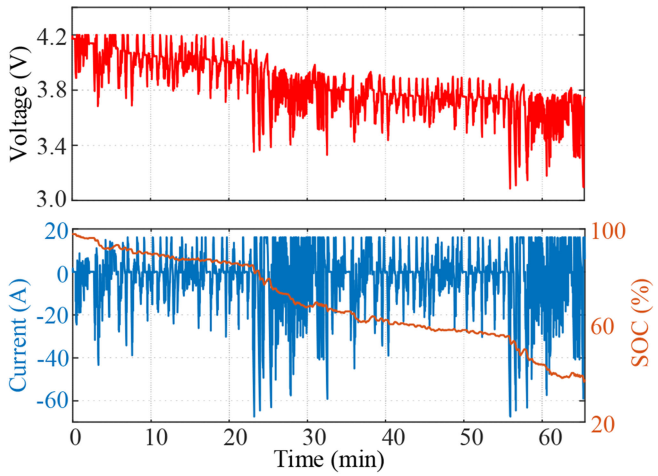

Fig. 13. Drive cycle-C: 12.5 C-rate @ 25 °C.

Significant ripples in the estimated SOC can be found in the DSMO method due to the large C-rate, and the convergence time is also much longer as 12.5 min than the proposed method.

Furthermore, a higher C-rate test (12.5 C) at 25 °C was implemented by using drive cycle-C. Compared to the drive cycle-B, the flat SOC-OCV region is covered by the drive cycle-C and can be used to evaluate the robustness to noises under the larger C-rate. Similarly, the EKF-RLS and DSMO coestimation methods are compared to the proposed scheme, while all tunable parameters of the three methods are the same as the previous ones. As shown in Fig. 15 and Table IV, the proposed method and the EKF-RLS have a faster convergence rate and lower SOC estimation errors than the DSMO method. While, the proposed estimation scheme is more accurate in the flat SOC-OCV region compared to the EKF-RLS method, which is similar to the comparative test by using drive cycle-A. The RMSE in the entire range, RMSE in the flat region, and MAE in the flat region of the proposed scheme are 1.627%, 1.57%, and 3.772%, respectively. The convergence time is around 12 s.

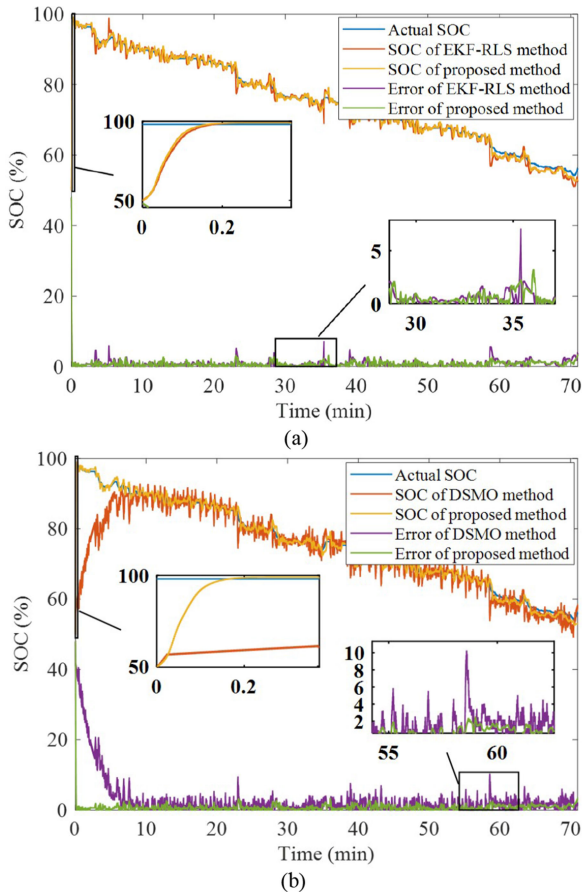

Fig. 14. Comparative experiments with conventional coestimation techniques (drive cycle-B: 10.2 C-rate @ 25 °C). (a) EKF-RLS. (b) Dual SMO.

TABLE III
RMSE AND MAE OF SOC ESTIMATION BY USING DRIVE CYCLE-B: 10.2 C-RATE AND 25 °C

Techniques	Convergence Time	RMSE (entire)	MAE (after convergence)
EKF-RLS [33]	12 sec	1.653	7.056
Dual SMO [32]	12.5 min	6.279	10.186
Proposed	12 sec	1.502	3.214

TABLE IV
THE RMSE AND MAE OF SOC ESTIMATION BY USING DRIVE CYCLE-C: 12.5 C-RATE AND 25 °C

Techniques	Convergence Time	RMSE (entire)	RMSE (flat)	MAE (flat)
EKF-RLS [33]	12 sec	1.864	2.633	5.436
Dual SMO [32]	12.5 min	6.470	2.485	8.967
Proposed	12 sec	1.627	1.570	3.772

Therefore, the proposed coestimation scheme shows better performance than conventional coestimation methods in different C-rate conditions and at different ambient temperatures.

The SOH estimation results of the proposed scheme in drive cycle-B and drive cycle-C are shown in Fig. 16. The capacity is

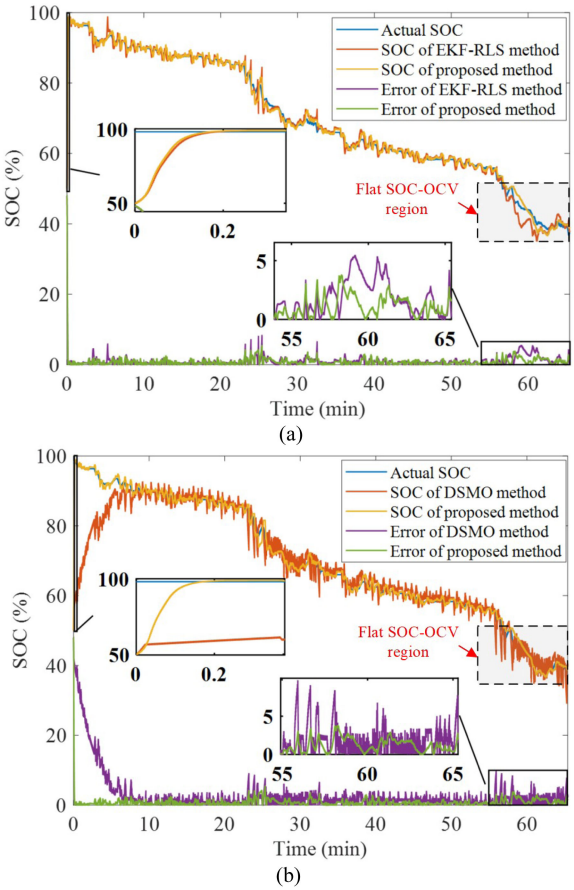

Fig. 15. Comparative experiments with conventional co-estimation techniques (drive cycle-C: 12.5 C-rate @ 25 °C). (a) EKF-RLS. (b) Dual SMO.

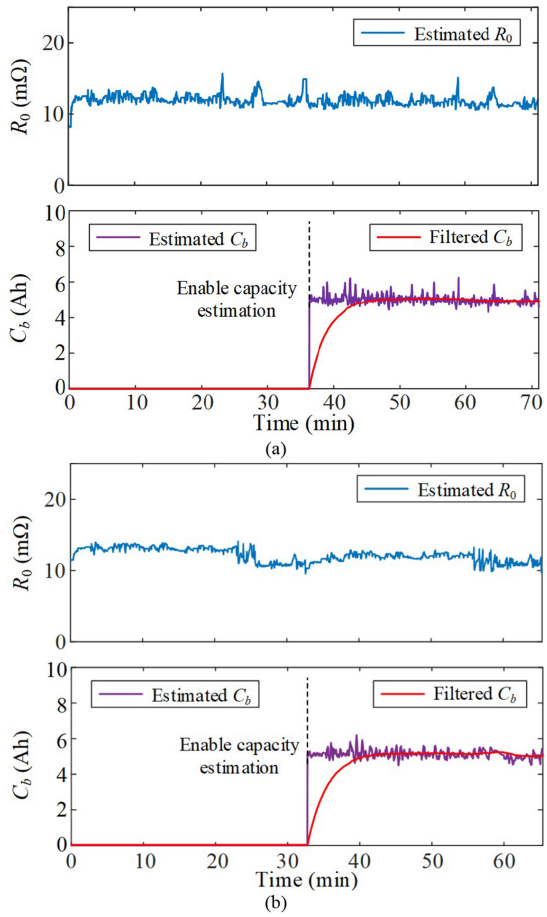

Fig. 16. SOH estimation results of the proposed scheme with high C-rate drive cycles @ 25 °C. (a) Drive cycle-B. (b) drive cycle-C.

TABLE V
CAPACITY ESTIMATION AT VARIOUS AGING LEVELS

Actual capacity (Ah)	5.4	5.13	5.1	4.95	4.35
Estimated capacity (Ah)	5.412	5.108	5.072	5.011	4.268
Error (Ah)	-0.012	0.022	0.028	-0.061	0.082

estimated by (14), which is isolated to the SOC and resistance estimation. As shown, the internal resistance R_0 and capacity C_b can be well estimated but containing some ripples due to the large C-rate. Since the capacity fade due to aging is slowly time-varying, a low-pass filter can be used for the capacity estimation to achieve ripple-free estimation and accurate aging diagnosis, which is shown in Fig. 16 as well.

Then, the capacity estimation results at different aging levels are summarized in Table V. The drive cycle-B and drive cycle-C are used for the battery cell to accelerate the battery aging due to the high C-rate current. The estimated capacity is derived by using the low-pass filter. As observed, the battery capacity from the fresh battery cell (5.4 Ah) to the end of life (4.35 Ah) can be well estimated.

VI. CONCLUSION

The article proposes a new SOC and SOH coestimation method with reduced coupling based on convex optimization. This numerical estimator can directly solve the SOC through the battery model, without the usage of Coulomb-counting method; and therefore, it avoids the strong coupling between the SOC and capacity estimations. Meanwhile, the internal resistance can be estimated by simply modifying the cost function, which is more compact and avoids the complicated design of observer network. Moreover, the detailed convex analysis proves the convergence of the proposed optimization on the whole state plane. In experiments, a 5.4 Ah Lithium polymer battery cell under a mixed drive cycle was used to validate the proposed method. The comparative study between the conventional and proposed methods verifies that the proposed strategy can offer good estimation accuracy of SOC and SOH.

REFERENCES

[1] B. Scrosati and J. Garche, "Lithium batteries: Status, prospects and future," *J. Power Source*, vol. 195, no. 9, pp. 2419–2430, 2010.
[2] J. Meng *et al.*, "An overview and comparison of online implementable soc estimation methods for lithium-ion battery," *IEEE Trans. Ind. Appl.*, vol. 54, no. 2, pp. 1583–1591, Mar./Apr. 2018.

[3] Y. Zhang, W. Song, S. Lin, and Z. Feng, "A novel model of the initial state of charge estimation for LiFePO4 batteries," *J. Power Sources*, vol. 248, pp. 1028–1033, 2014.
[4] K.-S. Ng, C.-S. Moo, Y.-P. Chen, and Y.-C. Hsieh. "Enhanced Coulomb counting method for estimating state-of-charge and state-of-health of lithium-ion batteries," *Appl. Energy*, vol. 86, no. 9, pp. 1506–1511, 2009.
[5] A. Nugroho, E. Rijanto, F. D. Wijaya, and P. Nugroho, "Battery state of charge estimation by using a combination of Coulomb counting and dynamic model with adjusted gain," in *Proc. Int. Conf. Sustain. Energy Eng. Appl.*, 2015, pp. 54–58.
[6] L. Languang, X. Han, J. Li, J. Hua, and M. Ouyang, "A review on the key issues for lithium-ion battery management in electric vehicles," *J. Power Sources*, vol. 226, pp. 272–288, 2013.
[7] Q. Wang, Y. He, J. Shen, X. Hu, and Z. Ma, "State of charge-dependent polynomial equivalent circuit modeling for electrochemical impedance spectroscopy of lithium-ion batteries," *IEEE Trans. Power Electron.*, vol. 33, no. 10, pp. 8449–8460, Oct. 2018.
[8] S. Rodrigues, N. Munichandraiah, and A.K. Shukla, "A review of state-of-charge indication of batteries by means of A.C. impedance measurements," *J. Power Source*, vol. 87, no. 1–2, pp. 12–20, 2000.
[9] S. Skoog and S. David, "Parameterization of linear equivalent circuit models over wide temperature and SOC spans for automotive lithium-ion cells using electrochemical impedance spectroscopy," *J. Energy Storage*, vol. 14, pp. 39–48, 2017.
[10] A. Zenati, P. Desprez, and H. Razik, "Estimation of the SOC and the SOH of Li-ion batteries, by combining impedance measurements with the fuzzy logic inference," in *Proc. IEEE 36th Annu. Conf. Ind. Electronics Soc.*, 2010, pp. 1773–1778.
[11] C. Burgos, D. Sáez, M. E. Orchard, and R. Cárdenas, "Fuzzy modelling for the state-of-charge estimation of lead-acid batteries," *J. Power Sources*, vol. 274, pp. 355–366, 2015.
[12] J. Meng, G. Luo, and F. Gao, "Lithium polymer battery state-of-charge estimation based on adaptive unscented Kalman filter and support vector machine," *IEEE Trans. Power Electron.*, vol. 31, no. 3, pp. 2226–2238, Mar. 2016.
[13] Z. Deng, L. Yang, Y. Cai, H. Deng, and L. Sun, "Online available capacity prediction and state of charge estimation based on advanced data-driven algorithms for lithium iron phosphate battery," *Energy*, vol. 112, pp. 469–480, 2016.
[14] J. C. Alvarez Anton, P. J. Garcia Nieto, C. Blanco Viejo, and J. A. Vilan Vilan, "Support vector machines used to estimate the battery state of charge," *IEEE Trans. Power Electron.*, vol. 28, no. 12, pp. 5919–5926, Dec. 2013.
[15] M. Charkhgard and M. Farrokhi, "State-of-charge estimation for lithiumion batteries using neural networks and EKF," *IEEE Trans. Ind. Electron.*, vol. 57, no. 12, pp. 4178–4187, Dec. 2010.
[16] H. Chaoui and C. C. Ibe-Ekeocha, "State of charge and state of health estimation for lithium batteries using recurrent neural networks," *IEEE Trans, on Veh. Technol.*, vol. 66, no. 10, pp. 8773–8783, Oct. 2017.
[17] E. Chemali, P. J. Kollmeyer, M. Preindl, R. Ahmed, and A. Emadi, "Long short-term memory networks for accurate state-of-charge estimation of li-ion batteries," *IEEE Trans. Ind. Electron.*, vol. 65, no. 8, pp. 6730–6739, Aug. 2018.
[18] J. Xu, C. C. Mi, B. Cao, J. Deng, Z. Chen, and S. Li, "The state of charge estimation of lithium-ion batteries based on a proportional-integral observer," *IEEE Trans. Veh. Technol.*, vol. 63, no. 4, pp. 1614–1621, May 2014.
[19] S. Muhammad, M. U. Rafique, S. Li, Z. Shao, Q. Wang, and N. Guan, "A robust algorithm for state-of-charge estimation with gain optimization," *IEEE Trans. Ind. Inform.*, vol. 13, no. 6, pp. 2983–2994, Dec. 2017.
[20] C. Zhang, K. Li, J. Deng, and S. Song, "Improved realtime state-of-charge estimation of LiFePO4 battery based on a novel thermoelectric model," *IEEE Trans. Ind. Electron.*, vol. 64, no. 1, pp. 654–663, Jan. 2017.
[21] A. Vasebi, M. Partovibakhsh, and S. M. T. Bathaee, "A novel combined battery model for state-of-charge estimation in lead-acid batteries based on extended Kalman filter for hybrid electric vehicle applications," *J. Power Source*, vol. 174, no. 1, pp. 30–40, 2007.
[22] A. Vasebi, S. M. T. Bathaee, and M. Partovibakhsh, "Predicting state of charge of lead-acid batteries for hybrid electric vehicles by extended Kalman filter," *Energy Convers. Manage.*, vol. 49, no. 1, pp. 75–82, 2008.
[23] M. Paschero *et al.*, "A novel mechanical analogy-based battery model for SOC estimation using a multicell EKF," *IEEE Trans. Sustain. Energy*, vol. 7, no. 4, pp. 1695–1702, Oct. 2016.
[24] R. Xiong, H. He, F. Sun, and K. Zhao, "Evaluation on state of charge estimation of batteries with adaptive extended Kalman filter by experiment approach," *IEEE Trans. Veh. Technol.*, vol. 62, no. 1, pp. 108–117, Jan. 2013.
[25] H. He, R. Xiong, X. Zhang, F. Sun, and J. Fan, "State-of-charge estimation of the lithium-ion battery using an adaptive extended Kalman filter based on an improved thevenin model," *IEEE Trans. Veh. Technol.*, vol. 60, no. 4, pp. 1461–1469, May 2011.
[26] J. Hana, D. Kima, and M. Sunwoob, "State-of-charge estimation of leadacid batteries using an adaptive extended Kalman filter," *J. Power Sources*, vol. 188, no. 2, pp. 606–612, Mar. 2009.
[27] M. Ye, H. Guo, R. Xiong, and Q. Yu, "A double-scale and adaptive particle filter-based online parameter and state of charge estimation method for lithium-ion batteries," *Energy*, vol. 144, pp. 789–799, Feb. 2018.
[28] C. Burgos-Mellado, M. E. Orchard, M. Kazerani, R. Cárdenas, and D. Sáez, "Particle-filtering-based estimation of maximum available power state in Lithium-Ion batteries," *Appl. Energy*, vol. 161, pp. 349–363, Jan. 2016.
[29] C. Hu, B. D. Youn, and J. Chung, "A multiscale framework with extended Kalman filter for lithium-ion battery SOC and capacity estimation," *Appl. Energy*, vol. 92, pp. 694–704, 2012.
[30] Y. Hua, A. C.-Arenas, N. Warner, and G. Rizzoni, "A multi time-scale state-of-charge and state-of-health estimation framework using nonlinear predictive filter for lithium-ion battery pack with passive balance control," *J. Power Sources*, vol. 280, pp. 293–312, Apr. 2015.
[31] Y. Feng, C. Xue, Q. Han, F. Han, and J. Du, "Robust estimation for state-of-charge and state-of-health of lithium-ion batteries using integral-type terminal sliding-mode observers," *IEEE Trans. Ind. Electron.*, vol. 67, no. 5, pp. 4013–4023, May 2020.
[32] I. Kim, "A technique for estimating the state of health of lithium batteries through a dual-sliding mode observer," *IEEE Trans. Power Electron.*, vol. 25, no. 4, pp. 1013–1022, Apr. 2010.
[33] P. Shen, M. Ouyang, L. Lu, J. Li, and X. Feng, "The co-estimation of state of charge, state of health, and state of function for lithium-ion batteries in electric vehicles," *IEEE Trans. Veh. Technol.*, vol. 67, no. 1, pp. 92–103, Jan. 2018.
[34] Y. Sun, M. Preindl, S. Sirouspour, and A. Emadi, "Unified wide-speed sensorless scheme using nonlinear optimization for IPMSM drives," *IEEE Trans. Power Electron.*, vol. 32, no. 8, pp. 6308–6322, Aug. 2017.
[35] S. Nalakath, Y. Sun, M. Preindl, and A. Emadi, "Optimization-based position sensorless finite control set model predictive control for IPMSMs," *IEEE Trans. Power Electron*, vol. 33, no. 10, pp. 8672–8682, Oct. 2018.
[36] X. Hu, H. Yuan, C. Zou, Z. Li, and L. Zhang, "Co-estimation of state of charge and state of health for lithium-ion batteries based on fractional-order calculus," *IEEE Trans. Veh. Technol.*, vol. 67, no. 11, pp. 10319–10329, Nov. 2018.
[37] M. Bakr, *Nonlinear Optimization in Electrical Engineering With Applications in Matlab*. London, U.K.: Inst. Eng Technol., ch. 7, 2013.
[38] X. Hu, S. Li, and H. Peng, "A comparative study of equivalent circuit models for Li-ion batteries," *J. Power Source*, vol. 198, pp. 359–367, 2012.

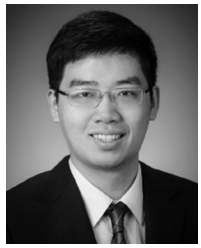

Dianxun Xiao (Student Member, IEEE) received the B.Eng. and M.Eng. degrees in electrical engineering from the Harbin Institute of Technology, Harbin, China, in 2016 and 2018, respectively. He is currently working toward the Ph.D. degree in electrical engineering with the McMaster Automotive Resource Centre, McMaster University, Hamilton, ON, Canada.

His current research interests including permanent magnet synchronous motor drives, switched reluctance motor drives, high-power converters, and battery management systems.

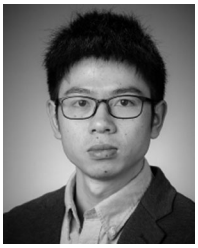

Gaoliang Fang received the B.S. and M.S. degrees in electrical engineering from the Northwestern Polytechnical University (NWPU), Xi'an, Shaanxi, China, in 2015 and 2018, respectively. He is currently working toward the Ph.D. degree in electrical engineering with the McMaster Automotive Resource Center (MARC), McMaster University, Hamilton, ON, Canada.

His research interests include torque control, vibration and noise reduction of switched reluctance machines, and sensorless control for permanent magnet synchronous machine.

Sheng Liu received the B.Eng. and M.Eng. degrees in electrical engineering from the McMaster University, Hamilton, ON, Canada, in 2018 and 2019, respectively.

His research interests include high power converters and power grids.

Shaoyi Yuan (Student Member, IEEE) received the B.Eng. degree in control engineering from the Northeastern University at Qinhuangdao (NEUQ), Qinhuangdao, China, in 2018. He is currently working toward the M.A.Sc. degree in electrical and computer engineering with the McMaster University, Hamilton, ON, Canada.

His research interests include grid-tied power converters, motor control, capacitor selection, and optimization for power electronics.

Ryan Ahmed (Member, IEEE) received the Ph.D. degree in mechanical engineering, with focus on mechatronics and EV control, from the McMaster University, Hamilton, ON, Canada, in 2014, the M.A.Sc. degree, with focus on artificial intelligence (AI) and fault detection, from the McMaster University, in 2011, and the M.B.A. degree in finance from the DeGroote School of Business, Hamilton, ON, Canada, in 2018.

He is currently an Adjunct Assistant Professor with the Department of Mechanical Engineering, McMaster University. He has taught several courses on Management and Control of Electric Vehicles at McMaster University, and at the educational EV/HEV boot camp at the IEEE Transportation Electrification Conference and Exposition (ITEC 2015), in Dearborn, MI, USA.

Dr. Ahmed is a Stanford Certified Project Manager and a certified Professional Engineer in Ontario. He was the recipient of the Best Paper Award at the IEEE Transportation Electrification Conference and Exposition, Dearborn, MI, USA, in 2012.

Saeid Habibi (Member, IEEE) received the Ph.D. degree in control engineering from the University of Cambridge, Cambridge, U.K., in 1990.

He spent a number of years in the industry as a Project Manager and Senior Consultant with Cambridge Control Ltd., Cambridge, U.K., and as a Senior Manager of Systems Engineering with AlliedSignal Aerospace, Toronto, ON, Canada. He is currently the Director of the Centre for Mechatronics and Hybrid Technology, and a Professor with the Department of Mechanical Engineering, McMaster University, Hamilton, ON, Canada. His academic background includes research into intelligent control, state and parameter estimation, fault diagnosis and prediction, variable structure systems, and fluid power. His current research interests include aerospace, automotive, water distribution, robotics, and actuation systems.

Dr. Habibi is on the Editorial Board of the Transactions of the Canadian Society of Mechanical Engineers, and is a Member of the American Society of Mechanical Engineers (ASME) and the ASME Fluid Power Systems Division Executive Committee. He was the recipient of two corporate awards for his contributions to the Allied Signal Systems Engineering Process, in 1996 and 1997. He was the recipient of the Institution of Electrical Engineers F.C. Williams Best Paper Award for his contribution to variable structure systems theory, in 1992, the Natural Sciences and Engineering Research Council (NSERC) Canada International Postdoctoral Fellowship at the University of Toronto, Toronto, ON, Canada, from 1993 to 1995, and the Boeing Visiting Scholar Sponsorship, in 2005.

Ali Emadi (Fellow, IEEE) received the B.S. and M.S. degrees in electrical engineering (with highest distinction) from the Sharif University of Technology, Tehran, Iran, in 1995 and 1997, respectively, and the Ph.D. degree in electrical engineering from Texas A&M University, College Station, TX, USA, in 2000.

He is the Canada Excellence Research Chair Laureate at McMaster University in Hamilton, Ontario, Canada. He is also the holder of the NSERC/FCA Industrial Research Chair in Electrified Powertrains and Tier I Canada Research Chair in Transportation Electrification and Smart Mobility. Before joining McMaster University, Dr. Emadi was the Harris Perlstein Endowed Chair Professor of Engineering and Director of the Electric Power and Power Electronics Center and Grainger Laboratories at Illinois Institute of Technology in Chicago, Chicago, IL, USA, where he established research and teaching facilities as well as courses in power electronics, motor drives, and vehicular power systems. He was the Founder, Chairman, and President of Hybrid Electric Vehicle Technologies, Inc. (HEVT)—-A university spin-off company of Illinois Tech Chicago, IL USA. He has authored and coauthored over 450 journal and conference papers as well as several books including *Vehicular Electric Power Systems* (2003), *Energy Efficient Electric Motors* (2004), *Uninterruptible Power Supplies and Active Filters* (2004), *Modern Electric, Hybrid Electric, and Fuel Cell Vehicles* (2009), and *Integrated Power Electronic Converters and Digital Control* (2009).

Dr. Emadi was the recipient of numerous awards and recognitions. He was the Advisor for the Formula Hybrid Teams at Illinois Tech and McMaster University, which won the GM Best Engineered Hybrid System Award at the 2010, 2013, and 2015 competitions. He is also the Editor for the *Handbook of Automotive Power Electronics and Motor Drives* (2005) and *Advanced Electric Drive Vehicles* (2014). He is the Co-Editor of the *Switched Reluctance Motor Drives* (2018). He was the Inaugural General Chair of the 2012 IEEE Transportation Electrification Conference and Exposition (ITEC) and has chaired several IEEE and SAE conferences in the areas of vehicle power and propulsion. He is the founding Editor-in-Chief for the IEEE TRANSACTIONS ON TRANSPORTATION ELECTRIFICATION.